

Vorticity and magnetic dynamo from subsonic expansion waves II: Dependence on magnetic Prandtl number, forcing scale, cooling time

Albert Elias-López^{1,2}, Fabio Del Sordo^{1,2,3} and Daniele Viganò^{1,2,4}

¹ Institute of Space Sciences (ICE-CSIC), Campus UAB, Carrer de Can Magrans s/n, 08193, Barcelona, Spain

² Institut d'Estudis Espacials de Catalunya (IEEC), 08034 Barcelona, Spain

³ INAF, Osservatorio Astrofisico di Catania, via Santa Sofia, 78 Catania, Italy

⁴ Institute of Applied Computing & Community Code (IAC3), University of the Balearic Islands, Palma, 07122, Spain

e-mail: albert.elias@csic.es

e-mail: delsordo@ice.csic.es

e-mail: daniele.vigano@csic.es

Received —; accepted —

ABSTRACT

Context. The amplification of astrophysical magnetic fields takes place via dynamo instability in turbulent environments. The presence of vorticity is crucial for the dynamo to happen. However, the role of vorticity is not yet fully understood.

Aims. This work is an extension of previous research on the effect of an irrotational subsonic forcing on a magnetized medium in the presence of rotation or a differential velocity profile, aimed at exploring a wider parameter space in terms of Reynolds numbers, magnetic Prandtl number, forcing scale, cooling timescale in a Newtonian cooling. We study the effect of imposing either the acceleration or the velocity forcing function to be curl-free and evaluate the terms responsible for the evolution vorticity.

Methods. We use Direct Numerical Simulations (DNS) to solve the fully compressible, resistive magnetohydrodynamical (MHD) equations with the Pencil Code. We study both isothermal and non-isothermal regimes and address the relative importance of different vorticity source terms.

Results. We report no small-scale dynamo for the models that do not include shear. We find a hydro instability, followed by a magnetic one, when a shearing velocity profile is applied. The vorticity production is found to be numerical in the purely irrotational case. Non-isothermality, rotation, shear or forcing in the form of a velocity curl-free, when included, contribute to increasing vorticity.

Conclusions. Consistently with our previous study, we find that turbulence driven by subsonic expansion waves can amplify vorticity and magnetic field only in the presence of a background shearing profile. The presence of a cooling function make the instability happens on a shorter timescale. We estimate critical Reynolds and Magnetic Reynolds Numbers of 40 and 20, respectively.

Key words. random expansion waves – shear – vorticity dynamo – dynamo – interstellar medium

1. Introduction

The occurrence of vortical flows is of high importance in all astrophysics due to their close connection with turbulence. Vorticity is in fact a way to characterize turbulent flows which are ubiquitous in astrophysical contexts. In turn, the connection between turbulence and the processes responsible for the amplification of astrophysical magnetic field still eludes a complete explanation. Magnetic fields are amplified at all scales in several astrophysical environments, from planets to the extragalactic medium. While the range of scales, densities and velocities is fairly wide, the instability responsible for the amplification of magnetic fields, known as dynamo, is thought to be active in all of these environments. Numerical models are commonly used to simulate many of these astrophysical contexts, from planets (e.g. Jones 2011) to galaxies (see e.g. Brandenburg & Ntormousi 2023, for a recent review), and in each of them the turbulence is injected through a forcing mechanism. We want here to concentrate on two questions that arise from these studies, namely (a) whether the occurrence of dynamo instability depends on the forcing mechanism, and (b) what are the minimum ingredients needed to trigger a dynamo in a magnetohydrodynamical turbulent medium.

In the attempt to address these two points, we expand on previous work (Mee & Brandenburg 2006; Del Sordo & Brandenburg 2011; Elias-López et al. 2023) that make use of a purely irrotational (i.e. curl-free) forcing of the velocity field to create a turbulent medium. The used forcing function mimics the occurrence of spherical expansion waves in an initially homogeneous medium, in a subsonic regime. The aforementioned studies found no vorticity amplification from the forcing alone in an isothermal purely hydrodynamical environment, and no dynamo amplification unless a background shearing profile is added to the system, independently of the equation of state. A similar result was obtained by Kahnishvili et al. (2012), who employed a curl-free forcing function for modelling of inflationary scenarios in the early universe. They found that the Lorentz force may produce some vorticity in isothermal models, but the magnetic field eventually dissipates without undergoing any kind of amplifications. Dosopoulou et al. (2012) found analogous results in the context of magnetized and rotating cosmological models. Nevertheless, other approaches found vorticity and magnetic fields to be exponentially amplified with a purely irrotational forcing added in the form of a stochastic function in Fourier space (e.g. Federrath et al. 2010; Achikanath Chirakkara et al. 2021; Seta

& Federrath 2022) even in isothermal contexts in the absence of large scale contributions to the forcing, such as rotation or shear. As a consequence, it remains not clear which are the minimum ingredients needed to excite a dynamo. It is possible that the difference between these different studies resides either in the used forcing function or in the exploration of different regions of a fairly wide parameter space, and this constitutes a motivation for the work presented here.

In the present paper we take as starting point the work done by Elias-López et al. (2023) and we perform an investigation of the effect played by varying the explosion width, the magnetic Prandtl number, as well as the use of a newtonian cooling function, on the amplification of vorticity and magnetic field. We also study the difference between forcing the turbulence by imposing an exactly irrotational forcing for the acceleration, or a variant which forces a locally fully potential velocity field and that hence may include vorticity creation by density fluctuations. The article is organized as follows. In section 2 we present the numerical model used to perform the study, in section 3 we describe the main results, and in section 4 we discuss some conclusions of our work.

2. Model and numerical methods

2.1. MHD equations with rotation and shear

We employ the same numerical models as in Elias-López et al. (2023), which for completion we briefly explain below. We use the public 3D MHD code Pencil Code¹ (Pencil Code Collaboration et al. 2021), which is a non-conservative, high-order, finite-difference code (sixth-order accurate in space and third-order Runge-Kutta in time). We solve the non-ideal fully-compressible MHD equations following an approach similar to what done by Del Sordo & Brandenburg (2011), that is either in a rigidly rotating frame, with angular velocity $\boldsymbol{\omega} = \Omega \mathbf{e}_z$, or with a differential velocity (shear) given by $\mathbf{u}^S = u_y^S(z) \mathbf{e}_y$, with $u_y^S = A \cos(kz)$, similar to Skoutnev et al. (2022); Käpylä et al. (2010); Käpylä et al. (2009). In our models z ranges from $-\pi$ to π , so when we include a shearing profile we set $k = 1$. This allows simple periodic boundary conditions in the three directions. While in Elias-López et al. (2023) we explored the role played by the shear amplitude, in the present work we use $A = 0.2$ in all the shearing cases.

The set of equations employed consists of the continuity equation, the momentum equation, the entropy equation (which we only solve for the non-isothermal/baroclinic case) and the induction equation, respectively:

$$\frac{D \ln \rho}{Dt} = -\nabla \cdot \mathbf{u}, \quad (1)$$

$$\frac{D\mathbf{u}}{Dt} = -\frac{\nabla p}{\rho} + \mathbf{F}_{visc} + \frac{\mathbf{J} \times \mathbf{B}}{\rho} - 2\boldsymbol{\Omega} \times \mathbf{u} + \mathbf{f} + \mathbf{f}_s, \quad (2)$$

$$T \frac{Ds}{Dt} = 2\nu \mathcal{S} \otimes \mathcal{S} + \rho^{-1} \nabla (c_p \rho \chi \nabla T) + \rho^{-1} \eta \mu_0 \mathbf{J}^2 - \frac{1}{\tau_{cool}} (c_s^2 - c_{s0}^2), \quad (3)$$

$$\frac{\partial \mathbf{A}}{\partial t} = \mathbf{u} \times (\nabla \times \mathbf{A}) + \eta \nabla^2 \mathbf{A}. \quad (4)$$

¹ <https://github.com/pencil-code>

In Eqs. 1-4 ρ is the mass density; $\mathbf{u}(t) = (\mathbf{u}^S + \mathbf{u}'(t))$ is the total velocity which can be thought of as the sum of shearing and turbulent velocities; p is the pressure; \mathbf{B} the magnetic field; \mathbf{A} its vector potential (i.e. $\mathbf{B} = \nabla \times \mathbf{A}$); $\mathbf{J} = (\nabla \times \mathbf{B})/\mu_0$ is the electrical current density (where μ_0 is the vacuum permeability); $\mathbf{F}_{visc} = \rho^{-1} \nabla \cdot (2\rho\nu\mathcal{S})$, where the traceless rate of strain tensor \mathcal{S} has components $S_{ij} = (1/2)(u_{i,j} + u_{j,i} - (1/3)\delta_{ij}\nabla \cdot \mathbf{u})$; \mathbf{f} the expansion wave forcing (see below for their definitions); χ is the thermal diffusivity; η is the magnetic diffusivity, c_{s0} is the initial, uniform sound speed (proportional to the initial temperature) and τ_{cool} is the cooling term timescale, introduced to avoid an indefinite heating. The advective derivative operator is $D/Dt := \partial/\partial t + \mathbf{u} \cdot \nabla$. The differential velocity profile is imposed directly on the y component of the total velocity by an amount proportional to the difference of velocity and the profile itself, so that u_y does not deviate much from the differential shearing profile:

$$\mathbf{f}_s = \frac{1}{\tau_S} (u_y^S - u_y) \hat{\mathbf{y}},$$

where we fix $\tau_S = 1$ (as for τ_{cool} for the entropy, the smaller the value, the more effective is the keeping u_y close to u_y^S).

In order to close the system of equations, we consider two types of equation of state (EoS): 1) a simple barotropic EoS $p(\rho) = c_s^2 \rho$, where we fix the value of the sound speed $c_s = 1$, or 2) an ideal EoS, dubbed also baroclinic case, $p(\rho, T) = \rho R_g T$, with R_g the specific gas constant and T the temperature; in this case, the sound speed squared is $c_s^2 = (\gamma - 1) c_p T$, where we fix the adiabatic index $\gamma = c_p/c_v = 5/3$ (corresponding to a monatomic perfect gas), and c_p and c_v are the specific heats at constant pressure and constant volume, respectively.

The forcing can be imposed in two different ways: either the acceleration itself is irrotational, as in Elias-López et al. (2023), or the force itself is irrotational, i.e. the spherical expansion takes into account density fluctuations. Both forcings are applied to the velocity field as accelerations but denote them \mathbf{f}_{acc} and \mathbf{f}_{mom} in order to distinguish them.

$$\mathbf{f}_{acc}(\mathbf{x}, t) = \nabla \phi(\mathbf{x}, t) = K \nabla e^{-(\mathbf{x} - \mathbf{x}_f(t))^2/R^2}, \quad \text{or} \quad (5)$$

$$\mathbf{f}_{mom}(\mathbf{x}, t) = \nabla \frac{\phi'(\mathbf{x}, t)}{\rho} = K' \nabla \frac{1}{\rho} e^{-(\mathbf{x} - \mathbf{x}_f(t))^2/R^2} \quad (6)$$

where: $\mathbf{x}_f(t)$ is the randomly changed expansion wave center, R is the radius of the Gaussian, $K = \phi_0 \sqrt{c_{s0} R / \Delta t}$ and $K' = \phi_0 \rho_0 \sqrt{c_{s0} R / \Delta t}$ are the corresponding normalization factors, Δt is the time interval after which a new expansion wave is forced in a new position (and it can be as short as the time-step). ϕ_0 controls the overall forcing amplitude and has dimensions of u^2 and ρ_0 is the mean density. In either case, the associated forcing representative wavenumber is thus $k_f = 2/R$.

The simulation domain consists of a uniform, cubic grid mesh $[-\pi, \pi]^3$, with triply periodic boundary conditions. We also study resolution convergence varying from 32^3 up to 256^3 mesh-points, and we find that 256^3 meshpoints are enough to assess our problem. We run some models at an even higher resolution, 512^3 to double check the validity of the results obtained at lower resolutions. However, simulations at this resolution are quite computationally expensive so we limited their use to double check numerical convergence. The chosen velocity profile allows simple periodic boundary conditions in the z direction if k is an integer. We adopt non-dimensional variables by measuring speed in units of the initial sound speed, c_{s0} , length in units

of $1/k_1$ where k_1 is the smallest wave number in the periodic domain, implying that the non-dimensional size of the domain is $(2\pi)^3$.

As the initial conditions: pressure and density are set constant and with value 1 throughout the box (making $\rho_0 = 1$ for all times), and so are entropy and temperature in the baroclinic case; the fluid is initially at rest so the flow is described by $\mathbf{u} = 0$; the initial magnetic field is a weak seed randomly generated with an amplitude of 10^{-6} in code units, uncorrelated at each point for the three components, corresponding to a $E_k \sim k^4$ power law, as reported by Mee & Brandenburg (2006).

2.2. Diagnostics

After an initial transitory phase, the simulations reach a stationary state, over the course of which the main average quantities maintain a saturated value. In particular, we will look at the root mean square of the total velocity, u_{rms} . In turn, this is used to define the fundamental timescale of our problem, that we will call turnover time, as

$$t_{turn} = (k_f u_{rms})^{-1}. \quad (7)$$

The turnover time can be understood as the average time for the fluid to cross an explosion width. In the cases where we employ the shearing profile we also use a similar definition with the shearing wavelength k and amplitude A :

$$t_{shear} = (kA)^{-1}. \quad (8)$$

The root mean square values of velocity u_{rms} and vorticity ω_{rms} (see Sec. 2.3) are used to define the following dimensionless numbers:

$$\begin{aligned} \text{Re} &= \frac{u_{rms}}{\nu k_f}, & \text{Rm} &= \frac{u_{rms}}{\eta k_f}, & \text{Re}_\omega &= \frac{\omega_{rms}}{\nu k_f^2}, \\ \text{Ma} &= \frac{u_{rms}}{c_s}, & \text{Pm} &= \frac{\nu}{\eta}, & k_\omega &= \frac{\omega_{rms}}{u_{rms}}, \end{aligned}$$

which are the Reynolds number, magnetic Reynolds number, vorticity Reynolds number, Mach number, magnetic Prandtl number, and a measure of vortical wavelength respectively.

2.3. Vorticity equation

To study the evolution of the vorticity ($\boldsymbol{\omega} = \nabla \times \mathbf{u}$), its sources or dissipative terms, we look at some diagnostic quantities derived from the terms of the vorticity evolution equation:

$$\begin{aligned} \frac{\partial \boldsymbol{\omega}}{\partial t} &= \nabla \times (\mathbf{u} \times \boldsymbol{\omega}) + \nabla \times \mathbf{F}_{visc} + \frac{\nabla \rho \times \nabla p}{\rho^2} + \nabla \times \left(\frac{\mathbf{J} \times \mathbf{B}}{\rho} \right) \\ &\quad - 2\nabla \times (\boldsymbol{\Omega} \times \mathbf{u}) + \nabla \times \mathbf{f} + \nabla \times \mathbf{f}_S. \end{aligned} \quad (9)$$

Here the first term on the right-hand side is analogous to the advective term $\nabla \times (\mathbf{u} \times \mathbf{B})$ in the induction equation, the second term represents the viscous forces acting on the system, the third is the baroclinic term, related to the EoS, the forth is the effect of the Lorentz force, the fifth appears if the system is rotating, the sixth is due to the effect of the implemented forcing and the last one regards the sinusoidal shearing profile.

Taking the dot product with $\boldsymbol{\omega}$, integrating over the volume, and using the vector identities $(\nabla \times \mathbf{a}) \cdot \mathbf{b} = \nabla \cdot (\mathbf{a} \times \mathbf{b}) + \mathbf{a} \cdot (\nabla \times \mathbf{b})$; $\nabla^2 \mathbf{a} = \nabla(\nabla \cdot \mathbf{a}) - \nabla \times (\nabla \times \mathbf{a})$ we obtain:

$$\begin{aligned} \frac{1}{2} \frac{\partial}{\partial t} \langle \omega^2 \rangle &= \langle (\mathbf{u} \times \boldsymbol{\omega}) \cdot \mathbf{q} \rangle - \nu \langle |\mathbf{q}|^2 \rangle + 2\nu \langle \mathbf{S} \nabla \ln \rho \cdot \mathbf{q} \rangle - \\ &\quad - \langle (\nabla T \times \nabla S) \cdot \boldsymbol{\omega} \rangle + \left\langle \frac{\mathbf{J} \times \mathbf{B}}{\rho} \cdot \mathbf{q} \right\rangle - 2\Omega \langle (\mathbf{e}_z \times \mathbf{u}) \cdot \mathbf{q} \rangle + \\ &\quad + \langle \mathbf{f} \cdot \mathbf{q} \rangle + \langle \mathbf{f}_S \cdot \mathbf{q} \rangle, \end{aligned} \quad (10)$$

where $\mathbf{q} = \nabla \times \boldsymbol{\omega}$. We do not time-evolve the vorticity itself, therefore we can address the numerical validity of the sum of terms as the total time derivative of $\langle \omega^2 \rangle$. We also use this diagnostic magnitudes to discriminate which are the most relevant vorticity amplification or destruction terms.

3. Results

The main result of our study is that, throughout our fairly wide exploration of the parameter space in terms of forcing scales (see sections 3.1 and 3.2), magnetic Prandtl number (section 3.3), cooling times (section 3.4) and Reynolds numbers, we do not obtain an HD or MHD instability unless a background shearing flow is imposed. This result holds both with a forcing acting on the momentum, as in Eq. 6, and on the velocity field alone, as in Eq. 5. The models including a shearing profile instead develop an exponential increase of vorticity, followed by an exponential increase of the magnetic field, unless the scale of the forcing is too small, as explained in 3.2. In section 2.3 we describe the contribution of vorticity source terms from Eq. 9. We list all runs with the shearing profile in A, and all models and the relative diagnostics in the tables added as supplementary materials.

3.1. Dependence on forcing scale without shear

We explored the role played by the forcing scale R by changing it alongside with ϕ_0 in order to reach a similar u_{rms} for all the models.

In the left panel of Fig. 1 we plot the temporal evolution of ω_{rms} in terms of turnover time for different, representative runs without rotation, with isothermal conditions. Independently of the forcing scale R , vorticity reaches a steady state after less than 15 turnover times, with the exception of the smallest value of $R = 0.10$, which takes less than 5 turnover times. In the model with a forcing scale of $R = 0.10$ we see the development of local transonic flows as a consequence of the attempt to reach values of the kinetic energy similar to the cases with larger forcing widths. This is accomplished by increasing the parameter ϕ_0 in Eq. 5 and it leads to a different behaviour of these models. The mean value of vorticity is observed to decrease with R , while its fluctuations do increase.

In the right panel of Fig. 1 we show the different kinetic spectra obtained from such runs. The corresponding forcing widths change the forcing wavelength k_f , thus changing the inertial range interval, as ν is kept constant. The slope of -2 seems to be independent of R , as already seen by Mee & Brandenburg (2006). No dynamo was observed in these runs in spite of having reached Rm larger than 200. When rotation is added the results are the similar to Elias-López et al. (2023), i.e. we obtain steeper slopes but similar inertial range behaviour than the non-rotating cases here plotted.

The latter statement can be seen more clearly in Fig. 2, where we plot the average of various diagnostics calculated during the saturated stage for the isothermal and baroclinic models, with or without rotation. Note that for $R = 0.1$ the non-isothermal

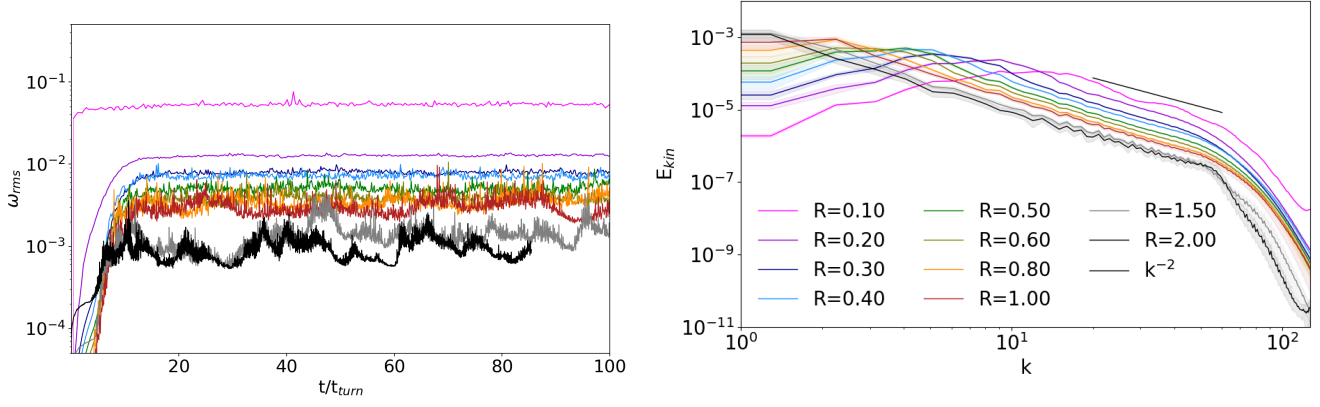


Fig. 1: Time evolution for ω_{rms} (left) and time-averaged kinetic spectra at saturation (right), for non-rotating isothermal runs with different explosion widths and similar total energy (see the tables in supplementary materials). Notice that the peaks in k are close to the corresponding forcing wavenumber $k_f = 2/R$.

runs are not shown because they reach locally supersonic flows and remain numerically stable for too few time-steps. Despite attempting to select a ϕ_0 which makes u_{rms} approximately independent of R , we could succeed in doing so only for the isothermal non-rotating case, while for the other non-isothermal or rotating cases u_{rms} mildly depends on R . Therefore, the more important dimensionless quantity is k_ω/k_f , as it is a measure of vorticity normalized with velocity and forcing wavelength. Figure 2 also illustrates many other features. First, we see how the Reynolds number increases with width for all cases, but no instability is found nevertheless. We notice that the non-rotating cases seem to have a lower overall ω , but it tends to growth with smaller R . In contrast, the rotating runs there is a maximum at $R = 0.4$, i.e. when expansion waves are about a fifth of the simulation domain, $k_f = 5$. We also see how isothermal rotating case show the highest values for ω_{rms} , u_{rms} and Re , but in k_ω/k_f they are closely matched by the non-isothermal rotating with the addition of a the thermal cooling time. As expected, the cooling term creates an additional source of dissipation, which we had to compensate by doubling the values of ϕ_0 (for $\tau_{cool} = 0.1$).

In Fig. 3 we plot the same quantities as in the left panel of Fig. 2, comparing runs with different resolutions and keeping R constant with a value of 0.5. Most quantities seem to be resolution independent even when we move to resolution low enough to erase a good part of the inertial ranges. We observe that u_{rms} is more or less resolution independent for all except two cases: (i) the isothermal non-rotating case, and (ii) the isothermal rotating case. The first case is compatible with the idea of vorticity being created solely by numerical sources.

As expected the contribution of rotation to ω is much greater than the baroclinic one in non-isothermal models, but this difference diminishes at small values of the forcing scale R . No dynamo is found either for the cases with rotation and/or non-isothermality with an ideal gas law and different cooling times. Thus the results of Elias-López et al. (2023) still hold when k_f grows nearly up to 1, and for Rm of several hundreds.

3.2. Dependence on forcing scale in the presence of shear

The general behaviour with the presence of shear is similar to the one found in Elias-López et al. (2023): a hydrodynamic instability develops first with an exponential growth of ω_{rms} which is then closely followed by a magnetic instability leading to an exponential amplification of b_{rms} . The complete set of runs with

the instability is in Table A.1 alongside with their diagnostics. After the linear phase of the dynamo a winding phenomena is seen for all cases, independently of R , Prandtl number and resolution. During this process B_y is further amplified in the shearing direction in a linear way, by winding. In Fig. 4 we plot both instabilities for the isothermal runs with different R .

The only case that does not develop a dynamo is that of very small forcing scale $R = 0.1$. In this case Re is perhaps subcritical, and this allows us to estimate a critical value of $Re \sim 40$ for the vorticity instability to take place. We find instead a critical magnetic Reynolds number of slightly less than 20 (see tabulated values) for the dynamo instability. We observe that both magnetic and kinetic helicities grow in the dynamo cases, and start oscillating when b_{rms} and ω_{rms} saturate. These oscillation resemble those seen in other instabilities such as the Tayler instability (e.g. Guerrero et al. 2019; Stefani et al. 2021; Monteiro et al. 2023).

3.3. Magnetic Prandtl number dependence

We observe only a weak dependence on Pm for the models that do not develop a dynamo instability. In the isothermal case we vary Pm from 0.25 up to 4 and see that Re_ω either increases with Pm in the absence of rotation, or slightly decrease with Pr , when rotation is added (see table 1). In the baroclinic case, Re_ω slightly decrease when $Pm = 4$ compared to the case of $Pm = 0.25$, independently on the presence of rotation. However, in the range of the explored values of Pr , we report a decrease of the initial magnetic field. Models with shear, conversely, develop a dynamo instability unless $Pm = 4$ or above (see tabulated values). We interpret this as a consequence of the lack of vorticity instability that does not develop when the physical viscosity increases above a certain value. The growth rates for the magnetic field increase with Pr , whilst the growth of vorticity is constant in the explored range.

We find that for $Pm = 0.1$ the vorticity is amplified, but, differently from the other cases, this instability is not followed by an exponential amplification of the magnetic field. This can be seen as a consequence of having a Rm below the critical value, since, in general, it is possible to excite a dynamo also at value of Pm below 0.1 (e.g. Warnecke et al. 2023)

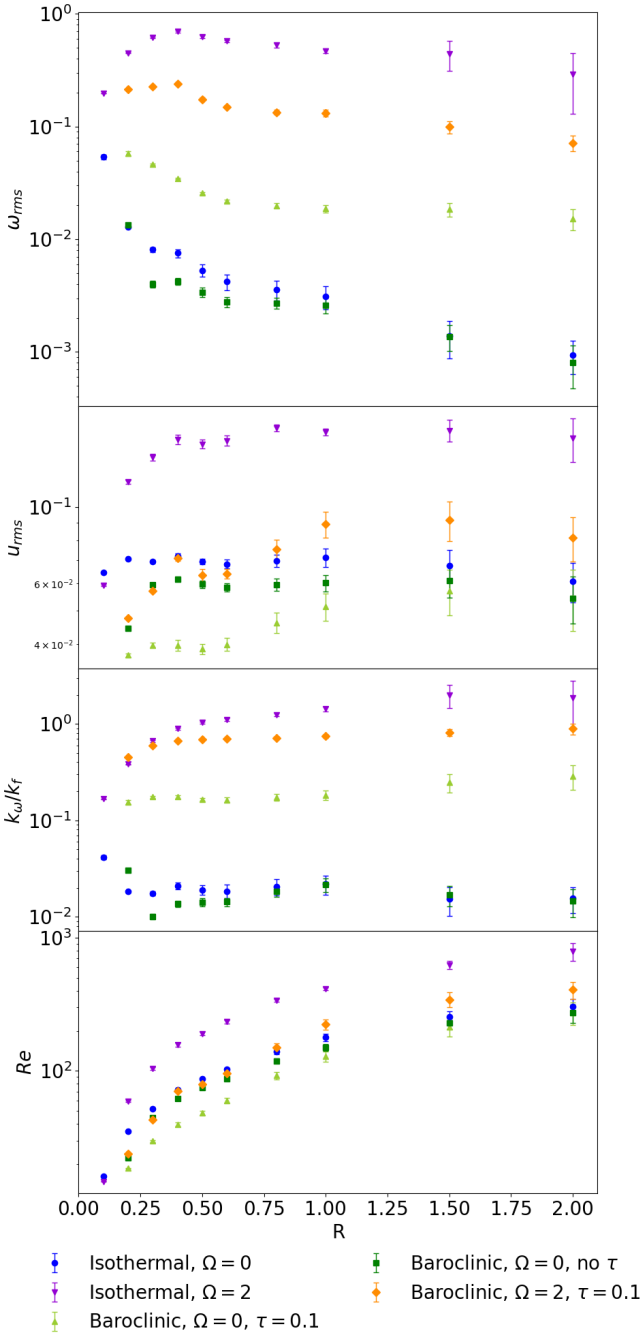


Fig. 2: Different diagnostic quantities, ω_{rms} , u_{rms} , k_ω/k_f and Re , from top to bottom, as a function of explosion width R . These runs have both Pm set to 1, i.e. $Rm=Re$, with a grid size of 256^3 and no dynamo present.

3.4. Dependence on cooling time

When the isothermal condition is relaxed we let the temperature evolve according to Eq. 3, where we use a Newtonian cooling term, regulated by the timescale τ_{cool} . The use of the cooling function leads to spectra cut at short wavelengths in models that does not develop instabilities. Differently, in the presence of shear and hence after a dynamo is excited, all the spectra recover their small-scale contribution and show again a wide dynamical range decreasing in a k^{-2} fashion down to a dissipation scale. However we observe that in the presence of this cooling term

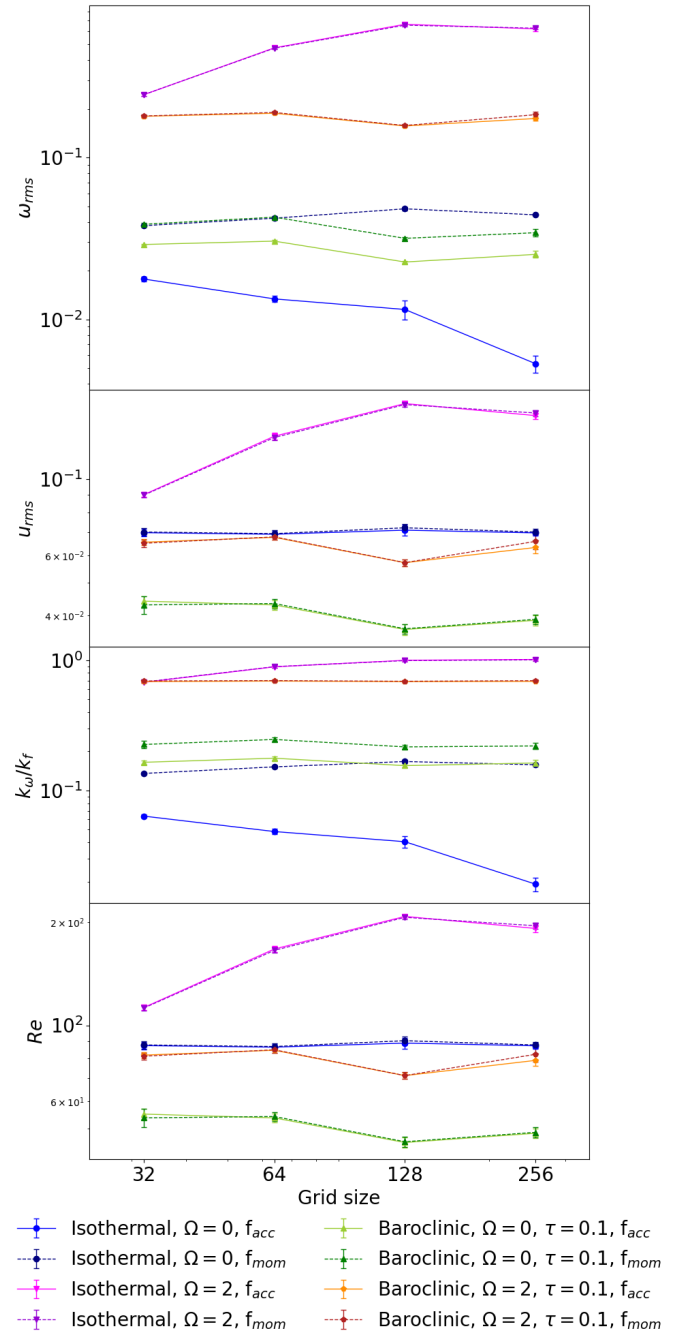


Fig. 3: Same magnitudes as in Fig. 2 but now for runs with $R = 0.5$, i.e. $k_f = 4$, different resolutions, and varying the type of forcing.

the instability kicks in at much earlier times, independently of the value of τ_{cool} , at least within the explored range. This can be seen as a quicker injection of vorticity in the system due to the cooling function. We observe that the average angle between ∇T and ∇s slightly increases when a cooling function is used, hence leading to a larger contribution of the baroclinic term in seeding the vorticity.

Another possible interpretation is to invoke an effect similar to what observed by Rädler et al. (2011). Irrotationally forced flows present peculiarities such as the possibility of having a negative magnetic diffusivity contribution from turbulent flows, especially at low Reynolds numbers, as shown analytically by

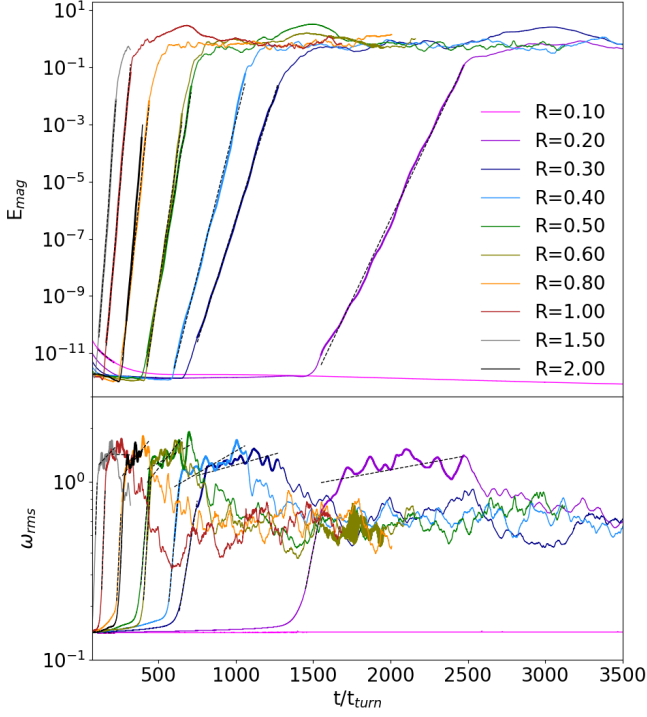


Fig. 4: Time evolution (in units of t_{turn}) of vorticity and magnetic energy of runs with the shearing profile and different R , see Table A.1. If we use the shearing timescales, the magnetic instability shows between 70 and 200 t_{shear} with more similar growth rates (see Fig. 5). In both cases, $R = 1.00$ and $R = 1.50$ take the least amount of time to reach the instability.

Table 1: Vorticity and magnetic field growth rates for different values of Pm . We show the values for ν and η , to better illustrate the different growths. We have not let the physical diffusivities reach numerical ones.

Pm	ν	η	$r(t_{turn}^{-1})$	$r_{\omega}(t_{turn}^{-1})$
0.1	$2 \cdot 10^{-4}$	$20 \cdot 10^{-4}$	-	$10.52 \cdot 10^{-3}$
0.25	$2 \cdot 10^{-4}$	$8 \cdot 10^{-4}$	$0.326 \cdot 10^{-2}$	$8.57 \cdot 10^{-3}$
0.5	$2 \cdot 10^{-4}$	$4 \cdot 10^{-4}$	$1.22 \cdot 10^{-2}$	$9.33 \cdot 10^{-3}$
0.75	$2 \cdot 10^{-4}$	$2.667 \cdot 10^{-4}$	$2.25 \cdot 10^{-2}$	$10.96 \cdot 10^{-3}$
1	$2 \cdot 10^{-4}$	$2 \cdot 10^{-4}$	$2.78 \cdot 10^{-2}$	$10.22 \cdot 10^{-3}$
1.25	$2.5 \cdot 10^{-4}$	$2 \cdot 10^{-4}$	$2.86 \cdot 10^{-2}$	$9.18 \cdot 10^{-3}$
1.5	$3 \cdot 10^{-4}$	$2 \cdot 10^{-4}$	$3.07 \cdot 10^{-2}$	$10.01 \cdot 10^{-3}$
2	$4 \cdot 10^{-4}$	$2 \cdot 10^{-4}$	$3.44 \cdot 10^{-2}$	$9.38 \cdot 10^{-3}$
4	$8 \cdot 10^{-4}$	$2 \cdot 10^{-4}$	-	-
10	$20 \cdot 10^{-4}$	$2 \cdot 10^{-4}$	-	-

Krause & Raedler (1980); Rädler & Rheinhardt (2007); Rädler et al. (2011). These contribution to the diffusivity coming from the turbulence may affect the occurrence of dynamo instability even when one moves towards higher values of the magnetic Reynolds number, a regime that is closer to that of astrophysical bodies. Rädler et al. (2011) found, with mean-field approaches based on the Second Order Correlation Approximation (SOCA), that a negative contribution to the magnetic diffusivity can come from the presence of turbulence in irrotational flows in the case of small Péclet numbers $Pe = uL/k$, where u , L , and k are typical velocity, lengthscale, and diffusivity of a system. In our case,

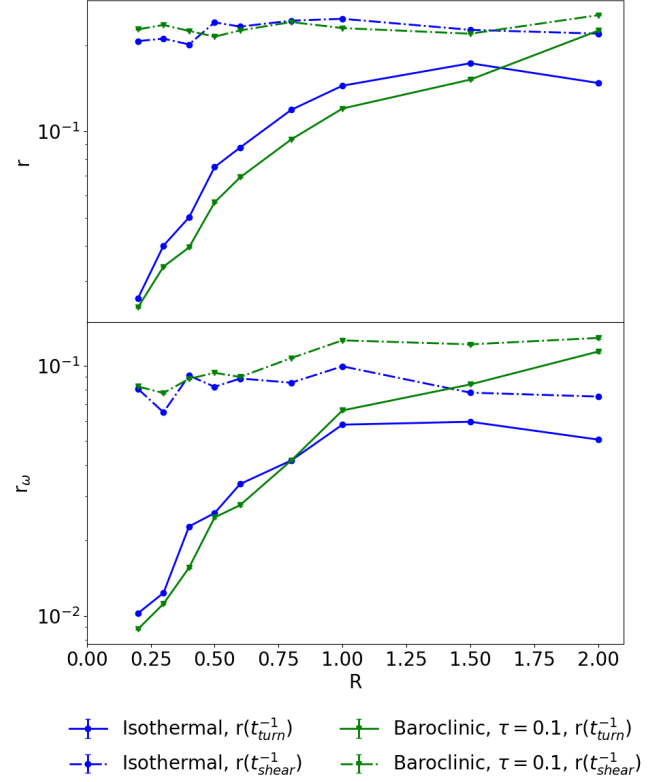


Fig. 5: Vorticity and magnetic energy growth rates as a function of explosion width R . The blue lines represent the isothermal models, while the green ones the baroclinic cases. The dashed lines, displaying an almost constant behaviour, are the calculation of the growth rates in terms of the shear typical timescale t_{shear} . We plot in the solid lines the results obtained in terms of the forcing turnover times, t_{turn} , which values are tabulated in the additional material.

the presence of a cooling time introduces an additional diffusion term for thermodynamical quantities, therefore Pe results to be smaller than in the absence of cooling. However, the SOCA approximation is valid only for small magnetic Reynolds numbers, which is a condition that is not satisfied in our models.

Although our cooling function is not meant to model any specific astrophysical environment, we can attempt a comparison with typical values of the cooling in the Interstellar Medium. Using the hydrogen cooling function Λ (e.g. Sutherland & Dopita 1993) and assuming a temperature of 10^4 K:

$$\log \frac{\Lambda}{\text{erg cm}^3 \text{s}^{-1}} (T = 10^4 \text{K}) \approx -22 \quad ; \quad \frac{\partial e}{\partial t} = \dots - \Lambda n$$

$$\rightarrow \tau_{cool} = \frac{k_B T}{\Lambda n} \approx 10^{10} \text{s} \approx 0.5 \text{ kyr}$$

If, as done by Elias-López et al. (2023), we consider a time unit of 8 Myr, then the cooling time τ_{cool} should be the order of 0.001. In our numerical models we can reach $\tau \sim 0.01$ which is one order of magnitude away from typical values of ISM.

3.5. Vorticity source terms

From Eq. 10 we can evaluate which are the most relevant terms in the vorticity equation for the different runs. We find that in the

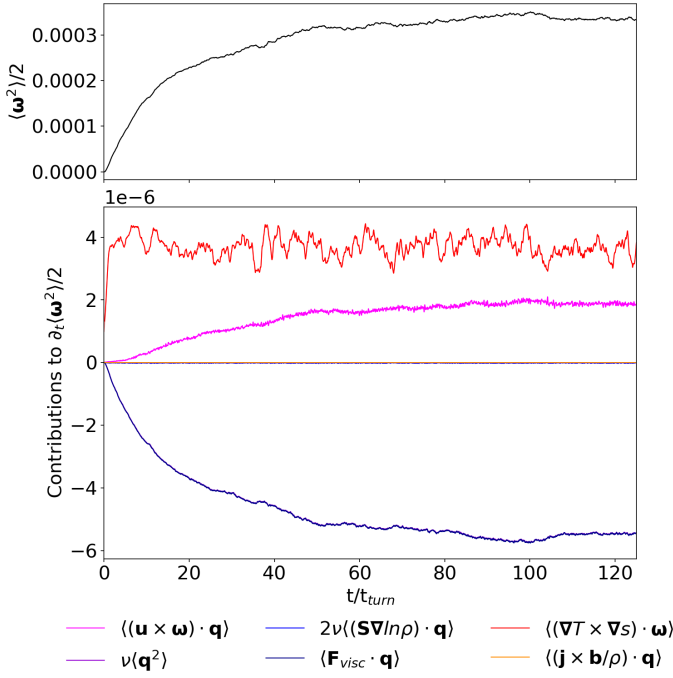


Fig. 6: Time evolution for $\omega_{rms}^2/2$ (left axis and gray line) and vorticity growth terms (right axis and various colored lines for each term) for a non-isothermal run with $R=0.5$ and forcing in acceleration form (and by construction its contribution to $\langle \partial_t \omega^2/2 \rangle$ is zero). This plot zooms on the beginning of the temporal evolution of all the terms until $t \approx 130 t_{turn}$. However the saturation regime does not present any relevant changes in time for more than $2000 t_{turn}$ and no instability is reached. Both $2\nu\langle \mathbf{S}\nabla\ln\rho \cdot \mathbf{q} \rangle$ and $\langle (\mathbf{j} \times \mathbf{b}/\rho) \cdot \mathbf{q} \rangle$ terms are negligible and very close to 0, so this makes the total contribution of viscous forces, i.e. $\langle \mathbf{F}_{visc} \cdot \mathbf{q} \rangle$, overlap with $\nu\langle \mathbf{q}^2 \rangle$.

isothermal non-rotating runs there are no positive terms comparable to the viscous ones. This fact along side the decrease of vorticity growth with resolution (see Fig. 3), makes us think that in such cases only numerical diffusive sources are in action, in agreement with what we already observed in Mee & Brandenburg (2006); Elias-López et al. (2023).

In Fig. 6 we can see the time series of the different source terms as a function of time, for a representative non-isothermal case. All terms are very small. The baroclinic term dominates as the most positive contribution. As vorticity grows, the turbulent contribution $\langle (\mathbf{u} \times \boldsymbol{\omega}) \cdot \mathbf{q} \rangle$ gains importance, and the sum of both are counteracted by viscous forces, so that ω_{rms} saturates. From the viscous contributions, only $\nu\langle \mathbf{q}^2 \rangle$ is relevant, while $2\nu\langle \mathbf{S}\nabla\ln\rho \cdot \mathbf{q} \rangle$ is more than one order of magnitude lower. This last statement holds true for all the isothermal, non-isothermal and rotating, non-rotating cases. Obviously, the Lorentz term is irrelevant in the cases without dynamo, orders of magnitude below by comparison.

When the forcing is exactly irrotational, its corresponding term does not contribute to vorticity generation. But when it is applied as in its second form (not exactly irrotational due to density fluctuations), there is indeed a small vorticity growth leading to similar behaviour in strength and shape to the baroclinic source term. When applying this type of forcing in the non-isothermal runs, the forcing vorticity growth overtakes the baroclinic term to such a point that this latter becomes negative.

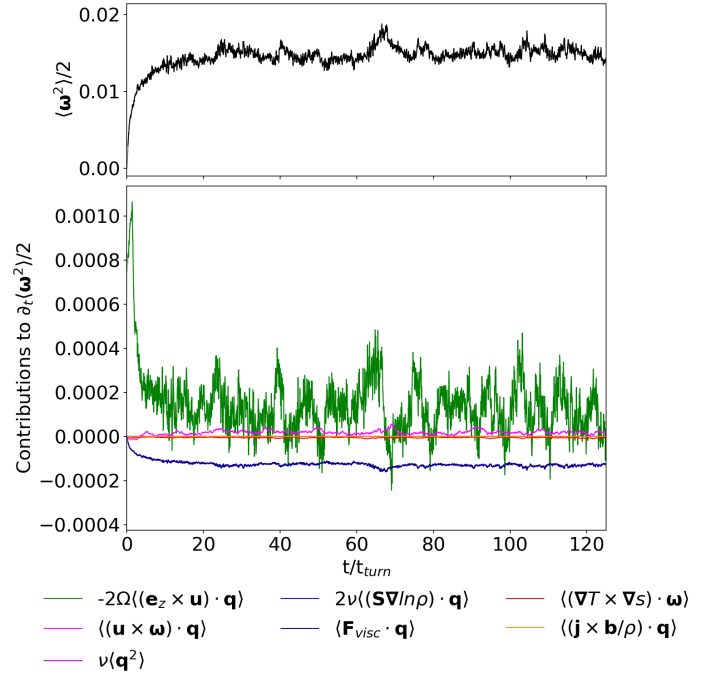


Fig. 7: Time evolution for $\omega_{rms}^2/2$ and vorticity growth terms for a non-isothermal rotating run with $R=0.5$ and forcing in acceleration form. The notation is the same as in Fig. 6, and similarly $2\nu\langle \mathbf{S}\nabla\ln\rho \cdot \mathbf{q} \rangle$ and $\langle (\mathbf{j} \times \mathbf{b}/\rho) \cdot \mathbf{q} \rangle$ overlap near 0, also making $\langle \mathbf{F}_{visc} \cdot \mathbf{q} \rangle$ overlap with $\nu\langle \mathbf{q}^2 \rangle$.

When the rotation is included, the vorticity generation is more relevant. In this case, the Coriolis source creates an amount of vorticity which is later counteracted by viscous terms, so that the steady state is reached. In Fig. 7 we show the same plot as in Fig. 6 but having added rotation. We can see that in the beginning the rotation term, $2\Omega\langle (\mathbf{e}_z \times \mathbf{u}) \cdot \mathbf{q} \rangle$, has a big positive spike which leads to the initial growth of vorticity. Note that it is larger than the baroclinic term in Fig. 6 by more than one order of magnitude and oscillates substantially even becoming negative at times, leading to an overall a noisier ω_{rms} . In the beginning of the run, the rotation contribution is mostly positive, and, when ω_{rms} saturates, the term is slightly positive in average, and of the same order of the viscous main contribution. Thus in the presence of rotation, all other source terms become much less important.

For the cases with the shearing profile the HD/MHD instability makes the contributions change substantially. In Fig. 8 we show all the relevant terms for a isothermal shearing run. As before, within the viscous forces $\nu\langle \mathbf{q}^2 \rangle$ still dominates over $2\nu\langle \mathbf{S}\nabla\ln\rho \cdot \mathbf{q} \rangle$, but this latter becomes more relevant in comparison to the cases described above.

The background shearing profiles increases ω_{rms} up to a certain values in a very few timesteps. This value is kept approximately until the vorticity instability kicks in (for example, until $t \approx 400 t_{turn}$ in Fig. 8). Afterwards, when vorticity is amplified, the advective term (which includes both shear and turbulence), $\langle (\mathbf{u} \times \boldsymbol{\omega}) \cdot \mathbf{q} \rangle$, brings the main positive contribution, as expected. The viscous forces are not enough to counteract this completely, thus leading to a growth of ω_{rms} .

The Lorentz term is negligible up to the point where dynamo starts. Then there is a brief time when it becomes slightly negative exactly when vorticity starts growing exponentially but still the dynamo has not kicked in. This behaviour was also observed

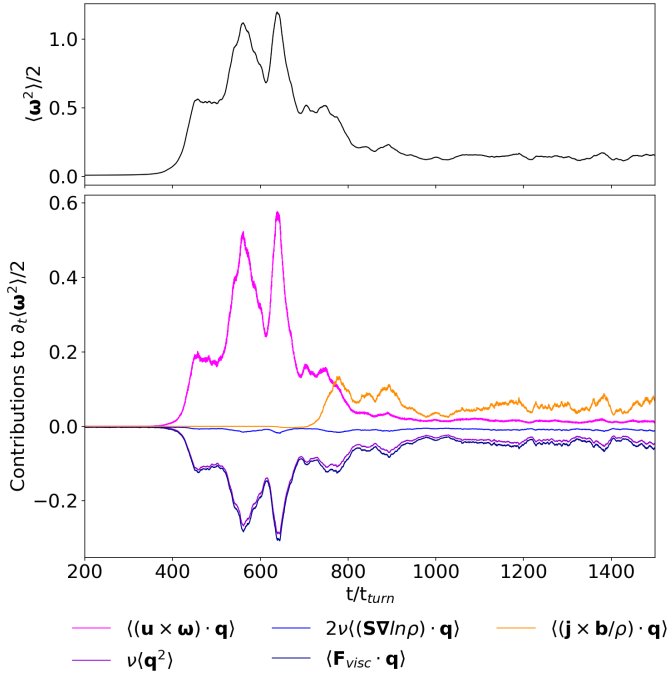


Fig. 8: Time evolution for $\omega_{rms}^2/2$ and vorticity growth terms for a isothermal run with the presence of shear, hence leading to instability, and with $R = 0.5$ and the exactly irrotational forcing. The notation is the same as in Fig. 6.

by Seta & Federrath (2022). When the kinetic phase of the dynamo starts, the Lorentz term increases but as the Lorentz forces act against the flow, $\langle(\mathbf{u} \times \boldsymbol{\omega}) \cdot \mathbf{q}\rangle$ decreases more than $\langle(\mathbf{j} \times \mathbf{b}/\rho) \cdot \mathbf{q}\rangle$ increases. This leads to a negative overall contribution and a decrease of vorticity, which later stabilizes at the end of the kinetic phase, and to the amplification of B_y by winding. In all dynamo runs the Lorentz term always ends up surpassing the advective term $\langle(\mathbf{u} \times \boldsymbol{\omega}) \cdot \mathbf{q}\rangle$.

4. Conclusion

This work is a continuation of Elias-López et al. (2023), and it aims at studying vorticity and dynamo instability in the presence of irrotationally forced turbulence. We first explored the role played by the scale on which the irrotational forcing is acting. We find that, independently on the scale of this forcing, no dynamo instability is developed for systems which do not include any shear. Also, whilst the root mean square values of vorticity weakly depend on the forcing scale, in no case we can observe an exponential amplification of vorticity. When shear is added to the picture, the vorticity is always exponentially amplified after a transient time if the kinematic viscosity is low enough, with the exception of the case of very small forcing scale, which does not lead to any growth during thousands of turnover times. Then it is followed by a dynamo instability if the magnetic diffusivity is not too high. By analyzing kinematic and magnetic power spectra we see how the typical scale of the system is provided by the forcing scale of the turbulence before the vorticity is amplified, and, conversely, by the scale of the shear, in the saturation phase. Based on that we observe that the growth rate of the dynamo depends on the scale of the expansion waves. The scale of the forcing sets also the time needed for the instability to develop. Models with a larger forcing scale amplify vorticity and magnetic fields after shorter times. The only models that imme-

diately develop the instability are those including both the baroclinic term and a cooling function. We observe an increase of one order of magnitude for the growth rate with the magnetic Prandtl number, which we varied between 0.1 and 10. We can extrapolate a critical value of the magnetic Reynolds number slightly lower than 20.

With these results in hands we can conclude that the presence of shear remains the basic ingredient for triggering a dynamo instability when subsonic turbulence is driven by spherical expansion waves. Future work will have to take into account turbulence forced on more than one scale at the same time as well as the role played by plane waves, before moving towards more complex models that can include density stratification and take into account also shocks and supersonic flows.

Acknowledgements. This work has been carried out within the framework of the doctoral program in Physics of the Universitat Autònoma de Barcelona and it is partially supported by the program Unidad de Excelencia María de Maeztu CEX2020-001058-M. DV and AE are supported by the European Research Council (ERC) under the European Union's Horizon 2020 research and innovation programme (ERC Starting Grant "IMAGINE" No. 948582, PI: DV). FDS acknowledges support from a Marie Curie Action of the European Union (Grant agreement 101030103). The authors acknowledge support from "María de Maeztu" award to the Institut de Ciències de l'Espai (CEX2020-001058-M). We are grateful to Axel Brandenburg, Matthias Rheinhardt, Eva Ntormousi, Federico Stasyszyn, Andrea Pallottini, Amit Seta and Claudia Soriano-Guerrero for fruitful discussions. We also want to acknowledge the whole Pencil Code community for support. AE gratefully acknowledges Scuola Normale Superiore for hospitality during October 2023. We acknowledge the use of the SCAYLE supercomputer of the Spanish Supercomputing Network, via project RES/BSC Call AECT-2023-2-0034 (PI FDS).

References

- Achikanath Chirakkara, R., Federrath, C., Trivedi, P., & Banerjee, R. 2021, *Phys. Rev. Lett.*, 126, 091103
- Brandenburg, A. & Ntormousi, E. 2023, *Annual Review of Astronomy and Astrophysics*, 61, 561
- Del Sordo, F. & Brandenburg, A. 2011, *A&A*, 528, A145
- Dosopoulou, F., Del Sordo, F., Tsagas, C. G., & Brandenburg, A. 2012, *Phys. Rev. D*, 85, 063514
- Elias-López, A., Del Sordo, F., & Viganò, D. 2023, *A&A*, 677, A46
- Federrath, C., Roman-Duval, J., Klessen, R. S., Schmidt, W., & Mac Low, M. M. 2010, *A&A*, 512, A81
- Guerrero, G., Del Sordo, F., Bonanno, A., & Smolarkiewicz, P. K. 2019, *MNRAS*, 490, 4281
- Jones, C. A. 2011, *Annual Review of Fluid Mechanics*, 43, 583
- Kahniashvili, T., Brandenburg, A., Campanelli, L., Ratra, B., & Tevzadze, A. G. 2012, *Phys. Rev. D*, 86, 103005
- Käpylä, P. J., Mitra, D., & Brandenburg, A. 2009, *Phys. Rev. E*, 79, 016302
- Krause, F. & Raedler, K. H. 1980, *Mean-field magnetohydrodynamics and dynamo theory*
- Käpylä, P. J., Korpi, M. J., & Brandenburg, A. 2010, *Monthly Notices of the Royal Astronomical Society*, 402, 1458
- Mee, A. J. & Brandenburg, A. 2006, *Monthly Notices of the Royal Astronomical Society*, 370, 415
- Monteiro, G., Guerrero, G., Del Sordo, F., Bonanno, A., & Smolarkiewicz, P. K. 2023, *MNRAS*, 521, 1415
- Pencil Code Collaboration, Brandenburg, A., Johansen, A., et al. 2021, *The Journal of Open Source Software*, 6, 2807
- Rädler, K.-H., Brandenburg, A., Del Sordo, F., & Rheinhardt, M. 2011, *Phys. Rev. E*, 84, 046321
- Rädler, K.-H. & Rheinhardt, M. 2007, *Geophysical and Astrophysical Fluid Dynamics*, 101, 117
- Seta, A. & Federrath, C. 2022, *MNRAS*, 514, 957
- Skoutnev, V., Squire, J., & Bhattacharjee, A. 2022, *MNRAS*, 517, 526
- Stefani, F., Stepanov, R., & Weier, T. 2021, *Sol. Phys.*, 296, 88
- Sutherland, R. S. & Dopita, M. A. 1993, *ApJS*, 88, 253
- Warnecke, J., Korpi-Lagg, M. J., Gent, F. A., & Rheinhardt, M. 2023, *Nature Astronomy*, 7, 662

Appendix A: Listed simulations with sinusoidal shear

The following tables contain the complete list of runs developing the instability, i.e. which have the differential shearing background profile. All other runs are tabulated in the additional material.

Table A.1: Models with sinusoidal shearing velocity profile. In every model we use $B_0 = 10^{-6}$ as seed field, $\Delta t = 0.02$ as interval between two different explosions, and an amplitude of the shearing profile $A = 0.2$. ND stands for the growth rates not determined, even though dynamo was present.

256 ³	ν	χ	η	τ_{cool}	A	ϕ_0	R	t_{tot}	t_{turn}	k_{ω}/k_f	$Re(Rm)$	Re_{ω}	u_{rot0}/u_{rot}	u_{rot}/u_{rot}	$r(t_{min})$	$r_{\omega}(t_{min})$
M_S_Pm0.1	$2 \cdot 10^{-4}$	-	$20 \cdot 10^{-4}$	-	0.20	1	0.2	4189.19	0.637	0.0915	78.5 (7.85)	7.849	0.819	0.899	-	$1.052 \cdot 10^{-2}$
M_S_Pm0.25	$2 \cdot 10^{-4}$	-	$8 \cdot 10^{-4}$	-	0.20	1	0.2	2277.66	0.635	0.0919	78.8 (19.7)	19.70	0.811	0.894	$3.261 \cdot 10^{-3}$	$8.573 \cdot 10^{-3}$
M_S_Pm0.5	$2 \cdot 10^{-4}$	-	$4 \cdot 10^{-4}$	-	0.20	1	0.2	3492.59	0.634	0.0912	78.9 (39.5)	39.46	0.810	0.873	$1.224 \cdot 10^{-2}$	$9.333 \cdot 10^{-3}$
M_S_Pm0.75	$2 \cdot 10^{-4}$	-	$2.667 \cdot 10^{-4}$	-	0.20	1	0.2	3927.51	0.634	0.0911	78.9 (59.2)	59.20	0.809	0.867	$2.254 \cdot 10^{-2}$	$1.096 \cdot 10^{-2}$
M_S_Pm1	$2 \cdot 10^{-4}$	-	$2 \cdot 10^{-4}$	-	0.20	1	0.2	3559.77	0.633	0.0910	78.9 (78.9)	78.94	0.806	0.861	$2.783 \cdot 10^{-2}$	$1.022 \cdot 10^{-2}$
M_S_Pm1.25	$2.5 \cdot 10^{-4}$	-	$2 \cdot 10^{-4}$	-	0.20	1	0.2	3965.97	0.636	0.0910	62.9 (78.6)	78.64	0.825	0.852	$2.861 \cdot 10^{-2}$	$9.176 \cdot 10^{-3}$
M_S_Pm1.5	$3 \cdot 10^{-4}$	-	$2 \cdot 10^{-4}$	-	0.20	1	0.2	3811.68	0.637	0.0910	52.3 (78.5)	78.50	0.817	0.865	$3.073 \cdot 10^{-2}$	$1.001 \cdot 10^{-2}$
M_S_Pm2	$4 \cdot 10^{-4}$	-	$2 \cdot 10^{-4}$	-	0.20	1	0.2	4765.49	0.640	0.0914	39.0 (78.1)	78.07	0.824	0.872	$3.438 \cdot 10^{-2}$	$9.378 \cdot 10^{-3}$
M_S_Pm4	$8 \cdot 10^{-4}$	-	$2 \cdot 10^{-4}$	-	0.20	1	0.2	4757.68	0.649	0.0922	19.3 (77.0)	76.99	0.848	-	-	-
M_S_Pm10	$20 \cdot 10^{-4}$	-	$2 \cdot 10^{-4}$	-	0.20	1	0.2	3340.23	0.672	0.0947	7.44 (74.4)	74.43	0.903	-	-	-
M_S_W0.10	$2 \cdot 10^{-4}$	-	$2 \cdot 10^{-4}$	-	0.20	2	0.10	3012.18	0.33	0.04733	37.5	1.775	0.888	-	-	-
M_S_W0.20	$2 \cdot 10^{-4}$	-	$2 \cdot 10^{-4}$	-	0.20	1	0.20	3332.61	0.63	0.09071	78.8	7.103	0.809	0.855	$2.616 \cdot 10^{-2}$	$1.022 \cdot 10^{-2}$
M_S_W0.30	$2 \cdot 10^{-4}$	-	$2 \cdot 10^{-4}$	-	0.20	0.52	0.30	4923.52	0.95	0.1372	118.2	15.98	0.818	0.861	$3.997 \cdot 10^{-2}$	$1.233 \cdot 10^{-2}$
M_S_W0.40	$2 \cdot 10^{-4}$	-	$2 \cdot 10^{-4}$	-	0.20	0.36	0.40	4867.96	1.26	0.1819	159.0	28.42	0.807	0.851	$5.017 \cdot 10^{-2}$	$2.273 \cdot 10^{-2}$
M_S_W0.50	$2 \cdot 10^{-4}$	-	$2 \cdot 10^{-4}$	-	0.20	0.24	0.50	4889.66	1.58	0.2275	197.5	44.37	0.818	0.861	$7.514 \cdot 10^{-2}$	$2.572 \cdot 10^{-2}$
M_S_W0.60	$2 \cdot 10^{-4}$	-	$2 \cdot 10^{-4}$	-	0.20	0.175	0.60	4992.11	1.90	0.2738	236.5	63.89	0.812	0.862	$8.791 \cdot 10^{-2}$	$3.361 \cdot 10^{-2}$
M_S_W0.80	$2 \cdot 10^{-4}$	-	$2 \cdot 10^{-4}$	-	0.20	0.118	0.80	4908.57	2.51	0.3607	319.3	113.5	0.812	0.846	$1.190 \cdot 10^{-1}$	$4.175 \cdot 10^{-2}$
M_S_W1.00	$2 \cdot 10^{-4}$	-	$2 \cdot 10^{-4}$	-	0.20	0.087	1.00	4918.58	3.08	0.4455	404.7	177.5	0.805	0.847	$1.444 \cdot 10^{-1}$	$5.803 \cdot 10^{-2}$
M_S_W1.50	$2 \cdot 10^{-4}$	-	$2 \cdot 10^{-4}$	-	0.20	0.048	1.50	1217.34	4.85	0.6884	579.9	399.1	0.804	0.840	$1.729 \cdot 10^{-1}$	$5.959 \cdot 10^{-2}$
M_S_W2.00	$2 \cdot 10^{-4}$	-	$2 \cdot 10^{-4}$	-	0.20	0.031	2.00	1333.81	3.48	0.4909	359.4	176.4	0.942	-	$1.476 \cdot 10^{-1}$	$5.058 \cdot 10^{-2}$
MB_S_W0.20	$2 \cdot 10^{-4}$	$2 \cdot 10^{-4}$	$2 \cdot 10^{-4}$	0.1	0.20	2	0.20	1710.04	0.68	0.1102	73.00	8.046	0.97	0.97	$2.433 \cdot 10^{-2}$	$8.832 \cdot 10^{-3}$
MB_S_W0.30	$2 \cdot 10^{-4}$	$2 \cdot 10^{-4}$	$2 \cdot 10^{-4}$	0.1	0.20	1.04	0.30	2307.15	1.02	0.1628	110.2	17.82	0.96	0.96	$3.377 \cdot 10^{-2}$	$1.116 \cdot 10^{-2}$
MB_S_W0.40	$2 \cdot 10^{-4}$	$2 \cdot 10^{-4}$	$2 \cdot 10^{-4}$	0.1	0.20	0.72	0.40	2401.10	1.35	0.2165	148.7	32.19	0.95	0.93	$3.942 \cdot 10^{-2}$	$1.556 \cdot 10^{-2}$
MB_S_W0.50	$2 \cdot 10^{-4}$	$2 \cdot 10^{-4}$	$2 \cdot 10^{-4}$	0.1	0.20	0.48	0.50	2444.66	1.68	0.2590	185.9	48.15	0.95	0.92	$5.656 \cdot 10^{-2}$	$2.470 \cdot 10^{-2}$
MB_S_W0.60	$2 \cdot 10^{-4}$	$2 \cdot 10^{-4}$	$2 \cdot 10^{-4}$	0.1	0.20	0.35	0.60	2448.34	2.02	0.3010	223.3	67.21	0.96	0.93	$6.921 \cdot 10^{-2}$	$2.768 \cdot 10^{-2}$
MB_S_W0.80	$2 \cdot 10^{-4}$	$2 \cdot 10^{-4}$	$2 \cdot 10^{-4}$	0.1	0.20	0.236	0.80	2407.49	2.64	0.3889	302.9	117.8	0.94	0.92	$9.382 \cdot 10^{-2}$	$4.174 \cdot 10^{-2}$
MB_S_W1.00	$2 \cdot 10^{-4}$	$2 \cdot 10^{-4}$	$2 \cdot 10^{-4}$	0.1	0.20	0.174	1.00	2342.14	3.25	0.4744	384.4	182.3	0.93	0.91	$1.202 \cdot 10^{-1}$	$6.614 \cdot 10^{-2}$
MB_S_W1.50	$2 \cdot 10^{-4}$	$2 \cdot 10^{-4}$	$2 \cdot 10^{-4}$	0.1	0.20	0.096	1.50	2421.20	4.80	0.6864	586.3	402.2	0.92	0.88	$1.516 \cdot 10^{-1}$	$8.403 \cdot 10^{-2}$
MB_S_W2.00	$2 \cdot 10^{-4}$	$2 \cdot 10^{-4}$	$2 \cdot 10^{-4}$	0.1	0.20	0.062	2.00	2421.66	6.44	0.9191	777.1	713.7	0.95	0.87	$2.245 \cdot 10^{-1}$	$1.137 \cdot 10^{-1}$
MB_S_W0.50_tau0005	$2 \cdot 10^{-4}$	$2 \cdot 10^{-4}$	$2 \cdot 10^{-4}$	0.005	0.20	0.48	0.50	1245.53	1.58	0.2232	198.4	44.28	0.81	0.77	$5.863 \cdot 10^{-2}$	$3.137 \cdot 10^{-2}$
MB_S_W0.50_tau001	$2 \cdot 10^{-4}$	$2 \cdot 10^{-4}$	$2 \cdot 10^{-4}$	0.01	0.20	0.48	0.50	1277.6	1.59	0.2258	196.1	44.27	0.84	0.80	$5.993 \cdot 10^{-2}$	$2.776 \cdot 10^{-2}$
MB_S_W0.50_tau005	$2 \cdot 10^{-4}$	$2 \cdot 10^{-4}$	$2 \cdot 10^{-4}$	0.05	0.20	0.48	0.50	1297.98	1.68	0.2362	187.5	44.28	0.92	0.88	$7.864 \cdot 10^{-2}$	$3.164 \cdot 10^{-2}$
MB_S_W0.50_tau01	$2 \cdot 10^{-4}$	$2 \cdot 10^{-4}$	$2 \cdot 10^{-4}$	0.1	0.20	0.48	0.50	1297.98	1.70	0.2410	183.7	44.28	0.95	0.93	$6.769 \cdot 10^{-2}$	$3.251 \cdot 10^{-2}$
MB_S_W0.50_notau	$2 \cdot 10^{-4}$	$2 \cdot 10^{-4}$	$2 \cdot 10^{-4}$	-	0.20	0.48	0.50	979.59	1.57	0.2225	199.0	44.29	0.79	0.81	$7.601 \cdot 10^{-2}$	$3.203 \cdot 10^{-2}$
MB_S_W0.20_notau	$2 \cdot 10^{-4}$	$2 \cdot 10^{-4}$	$2 \cdot 10^{-4}$	-	0.20	1	0.20	1769.62	0.65	0.0925	76.75	7.100	0.85	0.87	$3.255 \cdot 10^{-2}$	$9.601 \cdot 10^{-3}$
512 ³	ν	χ	η	τ_{cool}	A	ϕ_0	R	t_{tot}	t_{turn}	k_{ω}/k_f	$Re(Rm)$	Re_{ω}	u_{rot0}/u_{rot}	u_{rot}/u_{rot}	$r(t_{min})$	$r_{\omega}(t_{min})$
M_OA020_512	$2 \cdot 10^{-4}$	-	$2 \cdot 10^{-4}$	-	0.20	1	0.2	1606.63	0.64	0.091	78.5	7.10	0.83	-	0.0264	0.0107
M_OA020_512	$1 \cdot 10^{-4}$	-	$1 \cdot 10^{-4}$	-	0.20	1	0.2	1950.99	0.64	0.090	157.0	14.2	-	-	0.0348	0.0162
M_OA060_512	$2 \cdot 10^{-4}$	-	$2 \cdot 10^{-4}$	-	0.60	1	0.2	1642.89	1.98	0.281	227.3	6.39	-	-	0.0995	0.0323